Journal of Solid State Chemistry 182 (2009) 3041–3048

Contents lists available at ScienceDirect

Journal of Solid State Chemistry

journal homepage: www.elsevier.com/locate/jssc

Pressure-induced coordination changes in $LiBO_2$

Li Lei [a], Duanwei He [a,b,*], Kai He [a], Jiaqian Qin [a], Shanmin Wang [a]

[a] Institute of Atomic and Molecular Physics, Sichuan University, Chengdu 610065, China
[b] State Key Laboratory of Metastable Materials Science and Technology, Yanshan University, Qinhuangdao 066004, China

ARTICLE INFO

Article history:
Received 16 April 2009
Received in revised form
20 July 2009
Accepted 26 July 2009
Available online 7 August 2009

Keywords:
$LiBO_2$
High-pressure
Phase transition
Coordination change
Differential thermal analysis
Infrared absorption spectra

ABSTRACT

The coordination and structure changes in $LiBO_2$ have been studied at high pressure and temperature up to 5 GPa and 1500 °C using *in-situ* high-pressure differential thermal analysis, infrared absorption spectra and X-ray diffraction. The layer framework structure of α-$LiBO_2$ is found to be compressed easily along the direction of **c**-axis, resulting in the formation of tetra-coordinated BO_4 units. The phase transition boundaries between α- and γ-$LiBO_2$ as well as between amorphous $LiBO_2$ hydrate and γ-$LiBO_2$ have negative pressure–temperature slopes. The conditions for transformation from α- to γ-$LiBO_2$ are lower than that necessary to transform amorphous $LiBO_2$ hydrate to γ-$LiBO_2$. Moreover, the melting curve of $LiBO_2$ has also been determined and has a positive pressure–temperature slope. Upon quenching from high pressure, $LiBO_2$ may not contain $^{[3]}$B–O–$^{[3]}$B rings but contain more fraction of $^{[4]}$B units with increasing pressure.

1. Introduction

Alkali borate is an excellent basic flux in silicate analysis [1] and is one of the attractive materials for wide band-gap nonlinear optics because of its deep ultraviolet transparencies with mechanical durability and high optical damage thresholds [2,3]. Geophysically, a minor fraction of borate component in silicate magma may affect the geodynamics in Earth's interior where pressure-induced structural changes play an important role in the thermodynamics and transportation of the Earth's interior [4–6]. Therefore, understanding the structure and the coordination changes in alkali borate under high pressure not only helps elucidate the densification mechanism of ternary oxides but also is of importance to the dynamics of magmatic melts in the Earth's interior.

Lithium metaborate ($LiBO_2$), the simplest alkali borate, is considered to be a congruent compound of the Li_2O–B_2O_3 system [7]. Several types of $LiBO_2$ hydrate and anhydrous products can be found during the course of thermal dehydration of $LiBO_2 \cdot 8H_2O$ [7–10]. The process of dehydration is complicated and identification of dehydration products is still a controversial issue [7–10]. On heating, $LiBO_2 \cdot 8H_2O$ is firstly dehydrated to a lower hydrate $LiBO_2 \cdot 2H_2O$ below 100 °C [8]. The lithium metaborate dihydrate is stable to ~140 °C [7,8]. At a constant temperature of ~150 °C, an amorphous intermediate phase can be produced [8,9]. The amorphous phase is best regarded as a kind of intermediate hydrate whose water content is ~$0.3H_2O$ determined by DSC/TG measurements [8,9]. Previous studies show that the foamy amorphous phase contains BO_3, BO_4 groups and $^{[3]}$B–O–$^{[3]}$B rings in terms of B atom coordination [7,8]. At the temperature above ~190 °C, the dehydrated amorphous hydrate could crystallize into other poorly crystalline phases designated as $LiBO_2 \cdot xH_2O$, The value of x could be 0.5 or 0.3 depending on different thermal dehydration processes [8,9].

On further increase in the baking temperature to 600 °C, an anhydrous monoclinic α-$LiBO_2$ can be obtained [7–10]. The α-$LiBO_2$ lattice parameters are $a = 5.838$ Å, $b = 4.348$ Å, $c = 6.449$ Å, and $\beta = 115.12°$, space group is $P2_1/n$ and the density is 2.180 g/cm^3 [11]. The structure of monoclinic α-$LiBO_2$ contains endless chains of BO_3 triangles with Li–O bonds between chains, these chains being parallel to the **b**-axis, and the atoms of a chain are almost coplanar. The Li atom forms three Li–O bonds with one chain and one bond with each of the two neighboring chains [11,12]. Upon subjecting to a pressure of 3.5 GPa at 850 °C, the α-$LiBO_2$ undergoes a transformation from tri-coordinated ($^{[3]}$B) to tetra-coordinated boron ($^{[4]}$B), forming dense tetrahedral γ-$LiBO_2$, where both boron and lithium atoms are of four-coordination with oxygen [13]. The high-pressure phase, γ-$LiBO_2$, is quenchable, and has tetragonal symmetry with lattice parameter $a = 4.1961$ Å, $c = 6.5112$ Å, space group I-42d and a density of 2.882 g/cm^3 [14]. Pressure-induced coordination changes always occur in the similar compounds $LiMO_2$, where M can be the element of the group 13 of the Periodic Table, such as Ga [14] and Al [15].

* Corresponding author at: Institute of Atomic and Molecular Physics, Sichuan University, Chengdu 610065, China. Fax: +86 28 85466676.
E-mail address: duanweihe@yahoo.com (D. He).

0022-4596/$ - see front matter © 2009 Elsevier Inc. All rights reserved.
doi:10.1016/j.jssc.2009.07.060

The α-$LiBO_2$ is the high-temperature stable phase for $LiBO_2$ and the γ-$LiBO_2$ is the high-pressure stable phase. In terms of B atom coordination, amorphous $LiBO_2$ hydrate lies between α-$LiBO_2$ and γ-$LiBO_2$. It is unknown whether this kind of amorphous hydrate could directly crystallize into dense-phase γ-$LiBO_2$ at high pressure. The γ-$LiBO_2$ is known by now to be the densest phase in $LiBO_2$ system. Although it was reported that the irreversible transformation from α- to γ-$LiBO_2$ could occur at high pressure and temperature, the phase transition boundary between these two phases is still undefined. Besides using the high-pressure method, it was reported that γ-$LiBO_2$ can also be synthesized from glass at ambient pressure [16]. It has been observed that the α→γ phase transition could occur by isothermal heating of the glassy $LiBO_2$ at temperatures lower than 570 °C at ambient pressure [7]. On elevating the temperature above 600 °C, however, the γ-$LiBO_2$ could revert back to α-$LiBO_2$ [7,16]. The densification mechanism and the effect of pressure on $LiBO_2$ transformations have not been explored till now. It is still unknown whether α→γ phase transition at ambient condition has any intrinsic correlation with that at high pressure and temperature.

Under ambient pressure, the melting point of $LiBO_2$ is ~845 °C [7–9,17]. At high pressure, however, the melting behaviors of $LiBO_2$ have not been investigated, and the melting curve of $LiBO_2$ in *P–T* space has not been determined. The role of pressure on the coordination environment and structure in alkali borate glass remains an unsolved problem in solid-state chemistry, physics and material science. Previous studies show that the glassy $LiBO_2$ network consists mainly of local arrangements encountered in the α- and γ-$LiBO_2$ [18,19]. It is unclear whether the $LiBO_2$ glass quenched from melt under high pressure has any difference in coordination configuration with the one quenched under ambient pressure. Recent solid-state NMR studies on B_2O_3 glass quenched from melts at high pressures revealed that there are two densification mechanisms involved in the variation of boron species with pressure [20]. However, experiments on $LiBO_2$ glass quenched from melt at high pressure have not been reported. It is unclear whether a similar circumstance could exist in $LiBO_2$.

In order to gain further insight into the high-pressure behaviors of $LiBO_2$, here we investigated the pressure-induced bonding and structure changes in $LiBO_2$ by means of *in-situ* high-pressure differential thermal analysis (HP-DTA), combined with X-ray diffraction (XRD) as well as infrared absorption spectra (IR).

2. Experimental

The amorphous $LiBO_2$ hydrate and the α-$LiBO_2$ samples, which were used as starting materials in high-pressure experiments, were prepared by baking the hydrated $LiBO_2 \cdot 8H_2O$ for 6 h at 150 and 650 °C, respectively.

The high-pressure and high-temperature (HPHT) experiments were performed on a DS6 × 8MN cubic press. The high-pressure cell assembly was the same as the one in our previous study [15]. Tungsten carbide anvils were used to squeeze the pyrophyllite cell and generate high pressures up to 6 GPa in the sample. The pressure was calibrated by the aluminum melting-point method at high pressures [21]. The temperature was directly measured by Pt6%Rh–Pt30%Rh or NiCr–NiSi thermocouple. Different starting materials were, respectively, compacted in advanced into a disk shape (7.0 mm in diameter and 8.0 mm in height), placed in a capsule made of hBN, and then contained in the pyrophyllite high-pressure cell. The sample was first pressurized to certain pressure, heated to a desired temperature, kept at the HPHT conditions for at least 5 min, quenched at high pressure with the cooling rate about 50–60 °C/s, and then slowly decompressed at room temperature.

The *in-situ* HP-DTA experiments were carried out in the same large-volume cubic press described above. The high-pressure cell assembly in the HP-DTA experiments was a modification of that used in our previous study [15]. About 0.4 g high-purity $LiBO_2$ sample was compacted in advance into a disk shape (7.0 mm in diameter and 4.0 in height) and placed in the hexagonal BN (hBN) chamber. The hBN was chosen as the thermally inert reference material in this work owing to its excellent stability under our experimental conditions. Two NiCr–NiSi thermocouples were brought into the pressurized zone through a pyrophyllite pressure transmitting medium/gasket cube, dolomite cylindrical thermal insulator, graphite furnace, and hBN capsule to measure the temperatures in the sample and the thermally inert reference material (hBN). One thermocouple was placed at the center of $LiBO_2$ sample and the other one at the center of hBN. The thermocouple in hBN could monitor the temperature of the high-pressure cell, which was controlled by a programmed power controller. To avoid the direct contact of the thermocouples and the graphite furnace, thin hBN or ceramic tubes were used as electrical insulators. HP-DTA scans were run at a heating rate of 100 °C/min to a maximum temperature of 1300 °C after the pressure was elevated, and then followed by cooling at the same rate of 100 °C/min to room temperature before the pressure was released to ambient. The temperature of the samples and the differential thermal signal between the sample and the hBN were recorded by a multi-channel recorder. The starting materials as well as the treated samples were ground and characterized by means of IR absorption spectra and XRD. In order to confirm the studied phase transition has already taken place, the sample was immediately quenched from HPHT and then was taken to analyze right now after the needed DTA peaks appeared.

3. Results and discussion

Fig. 1 presents typical XRD patterns for the α-$LiBO_2$, the amorphous $LiBO_2$ hydrate and the samples recovered from different pressure–temperature (*P–T*) conditions. As observed in previous studies [13,14], α-$LiBO_2$ undergoes an irreversible structural transition to γ-$LiBO_2$ at 2.5 GPa and 300 °C (or higher *P–T* conditions). The minimum condition for the α→γ transition is

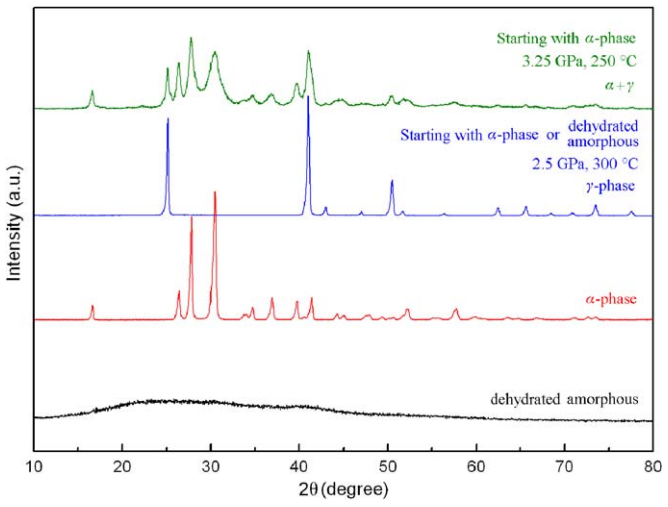

Fig. 1. Typical XRD patterns for the α-$LiBO_2$, the dehydrated amorphous $LiBO_2$ and the samples recovered from 2.5 GPa and 300 °C, 3.25 GPa and 250 °C.

lower than that reported by Marezio and Remeika (3.5 GPa, 850 °C) [13,14]. If we vary the treated condition to 3.25 GPa and 250 °C, it is found that α- and γ-$LiBO_2$ coexist in a recovered sample. Upon using amorphous $LiBO_2$ hydrate as the starting material, tetragonal γ-$LiBO_2$ can also be obtained after being quenched from 2.5 GPa and 300 °C (or higher *P–T* conditions), but the sample treated at 3.25 GPa and 250 °C is still amorphous. From the structural point of view, the B atom is three-fold coordinated in the monoclinic α-$LiBO_2$, and three- and four-fold coordinated in the amorphous $LiBO_2$ hydrate, but the coordination number for B changes from three-fold to four-fold in tetragonal γ-$LiBO_2$ after high-pressure treatment. Considering the unique structural difference between α-$LiBO_2$ and γ-$LiBO_2$, IR absorption spectroscopy can help differentiate cation coordination environments and identify the nature of coordination changes present in crystalline and amorphous lithium metaborate phases, where conventional XRD technique cannot work.

Fig. 2 presents the IR absorption spectra of α-$LiBO_2$, γ-$LiBO_2$ and amorphous $LiBO_2$ hydrate. Previous studies [18,22–27] on the vibrational spectra of a series of doped and undoped alkali borate glasses and crystals have summarized the occurrence of peaks in the following three regions, the broad absorption region 1150–1450 cm^{-1} is attributed to B–O bond stretching of trigonal BO_3 units, while that in the region 800–1100 cm^{-1} originates from B–O bond stretching of tetrahedral BO_4 units, and that between 400 and 800 cm^{-1} to the integrated vibrational peak of BO_3, BO_4 and LiO_4 groups. More exactly, the band located at ~760 cm^{-1} is from the interaction between LiO_4 and BO_4 group, and ~730 cm^{-1} is assigned to the bond bending vibration of B–O–B linkage of the B–O network; the band at ~490 cm^{-1} is assigned to vibration of the LiO_4 group, and the band at ~420 cm^{-1} is attributed to vibration of Li–O network in α-$LiBO_2$ crystal. On the basis of the above assignments, IR absorption spectra can probe the relative numbers of BO_4 and BO_3 units more directly than Raman spectra do.

Taking into account the difference in absorption regions for the tri-coordinated and tetra-coordinated boron, it can be deduced from Fig. 2 that there exist BO_4 groups and BO_3 groups in the amorphous $LiBO_2$ hydrate. It can be seen that the IR absorption peaks of amorphous $LiBO_2$ hydrate at 400–800 cm^{-1} are relatively weak in comparison to those for crystalline α- and γ-$LiBO_2$. This is due to the fact that, during the dehydration process, the framework of crystalline $LiBO_2 \cdot 2H_2O$ is broken down; however, at relatively low baking temperature (150 °C), the long-range atomic rearrangement is very difficult to occur owing to lack of sufficient thermal energy for overcoming potential barrier associated with the reconstructive transformation of crystalline $LiBO_2$. Hence that it may lead to the formation of the dehydrated amorphous material. In amorphous state, the linkages between networks are less than that in the crystal state, resulting in the relatively weak absorption bands in the region 400–800 cm^{-1}. We also notice that, the band at ~1250 cm^{-1}, which is not observed in the spectra of crystalline α- and γ-$LiBO_2$ but can be observed in those of glassy B_2O_3 and glassy $LiBO_2$ prepared by quenching melts [18], appears in the IR absorption spectra of amorphous $LiBO_2$ hydrate. According to previous IR spectra investigations [27,28], this band should come from B–O stretching vibrations in BO_3 units from $^{[3]}$B–O–$^{[3]}$B rings.

Fig. 3a presents the XRD patterns of α-$LiBO_2$ treated at different pressures and room temperature. The XRD peaks are found to be gradually broadened with increasing pressure. XRD peak broadening can be caused by reduction in grain size and lattice distortion (presence of micro-strain or macro-strain) in the sample [29]. Since the obtained XRD patterns are collected from the finely ground powder of the recovered samples, the macro-strain may not contribute to the peak broadening. The full-width at half-maximum (FWHM) can quantify the broadening of the

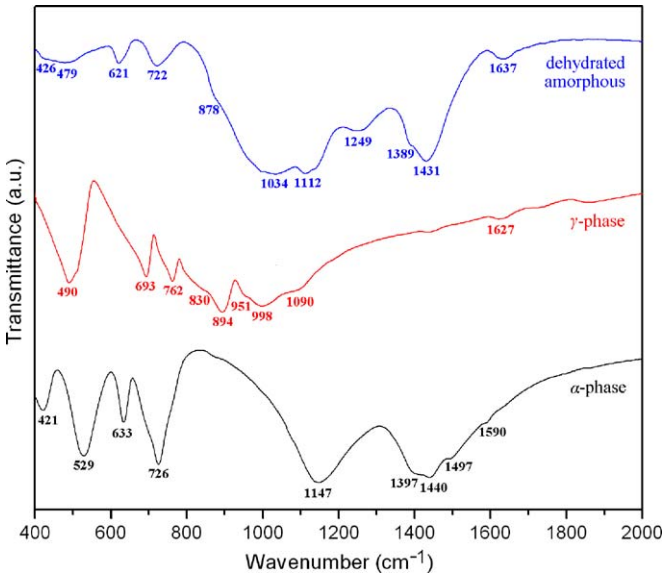

Fig. 2. IR absorption spectra for α-$LiBO_2$, γ-$LiBO_2$ and dehydrated amorphous $LiBO_2$.

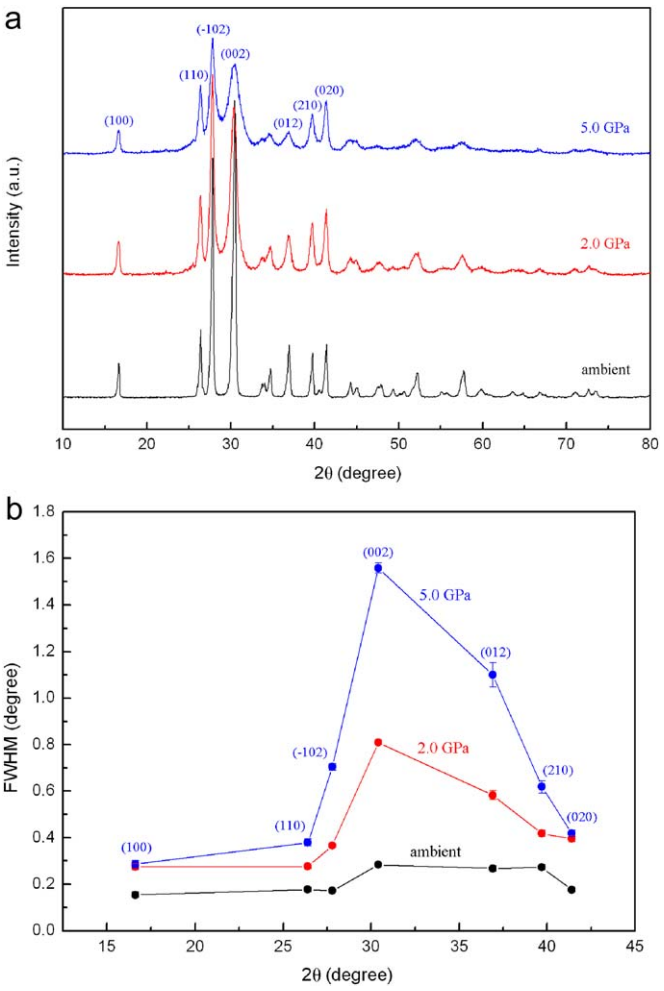

Fig. 3. (a) XRD patterns for α-$LiBO_2$ samples at ambient conditions as well as treated at 2.0 and 5.0 GPa. (b) The full-width at half-maximum (FWHM) of selected diffraction peaks for the α-$LiBO_2$ samples at ambient conditions as well as treated at 2.0 and 5.0 GPa.

peaks. Fig. 3b shows FWHM of selected diffraction peaks for the treated α-$LiBO_2$ samples. The FWHM of the (002) peak significantly increases with increase in pressure, but only slightly increases in the (100) and (020) FWHMs. The (002) peak, the main XRD peak of α-$LiBO_2$, is more liable to be affected by compression, and there is no linear relationship between FWHM and the peak position. Therefore, the average grain size reduction cannot be analyzed using Scherrer's equation [29], and the contribution of grain size reduction can be neglected for peak broadening. The broadening selectivity for peak should result from the structural inhomogeneity and lattice distortion induced by micro-strain in the samples. For further insight, the corresponding IR spectra for the treated α-$LiBO_2$ samples are shown in Fig. 4. As can be seen from the spectra, three absorption peaks in the 800–1100 cm^{-1} region (highlight in yellow) appear in the IR absorption spectra of the high-pressure recovered samples, and the intensity of these peaks increases with increase in pressure. The appearance of these absorption peaks suggests that the α-$LiBO_2$ (with only BO_3 groups) and some kind of amorphous $LiBO_2$ (with BO_3 and BO_4 groups) might coexist in the recovered sample, and the content of the amorphous $LiBO_2$ phase increases with increase in pressure. Also, the particular structure of the α-$LiBO_2$ contains endless chains of BO_3 triangles along the direction of the **b**-axis with Li–O bonds between each chain. If we view along the **b**-axis, as illustrated in Fig. 5, the atoms of each chain are very nearly coplanar, and each chain is nearly parallel. Previous *in-situ* high-temperature XRD study indicates that the **c**-axis exhibits the largest thermal expansive effect compared to **a** and **b** axes [8]. In this work, we find that the layered framework can be compressed easily along the direction of **c**-axis with increase in pressure, the parallel BO_3 chains are weakened and there is loss of long-range order, some of the atoms in neighboring chains are rearranged and form tetra-coordinated BO_4 groups ($BO_3 \rightarrow BO_4$), which can be easily detected by IR absorption spectra. The appearance of BO_4 groups may inevitably cause lattice distortion induced by micro-strain in the trigonal framework of α-$LiBO_2$. According to the above-described densification mechanism, the selective broadening of the XRD peaks for high-pressure-treated α-$LiBO_2$, as shown in Fig. 3b, is probably associated with the local distribution of the pressure-induced BO_4 groups in the layer-like framework of α-$LiBO_2$. The pressure-induced short-range atomic rearrangement in α-$LiBO_2$ may be the threshold of the complete densification to the higher coordinated structure (γ-$LiBO_2$).

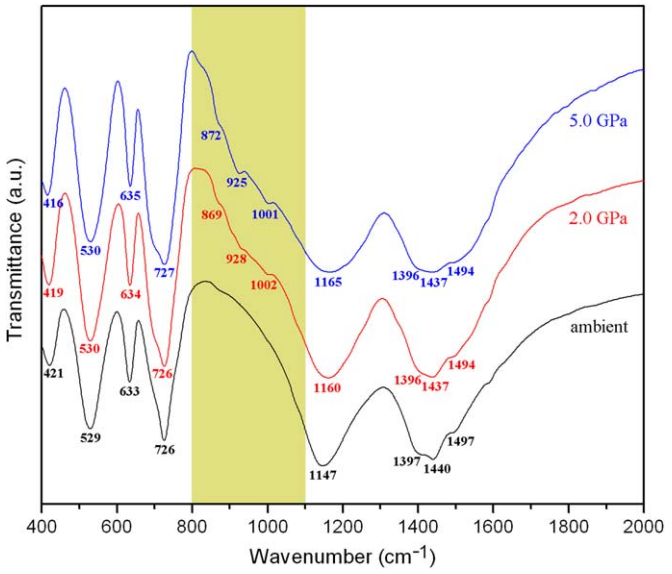

Fig. 4. IR absorption spectra for α-$LiBO_2$ samples at ambient conditions as well as treated at 2.0 and 5.0 GPa. (For interpretation of the references to colour in this figure legend, the reader is referred to the web version of this article.)

Pressure can induce the formation of denser forms with higher coordination number. At room temperature, α-$LiBO_2$ does not transform to γ-$LiBO_2$ at pressures below 5 GPa. In order to study thermodynamics of first-order phase transition in $LiBO_2$, an *in-situ* HP-DTA was used to monitor the temperature at which the first-order phase transition of $LiBO_2$ was triggered at high pressure. Fig. 6a presents the HP-DTA curves in the vicinity of structural transition from α- to γ-$LiBO_2$ at different pressures. As can be seen, DTA exothermic peaks shift towards lower temperature at higher pressures, indicating a lower transition temperature. The $^{[3]}B$ to $^{[4]}B$ conversion is kinetically preferred at high pressure. Upon using amorphous $LiBO_2$ hydrate as the starting material for HP-DTA experiments, the amorphous $LiBO_2$ hydrate directly crystallizes into densest crystalline state γ-$LiBO_2$ at high pressure, which is also an irreversible process evidenced by *ex-situ* XRD. Fig. 6b shows the HP-DTA curves in the vicinity of structural transition from dehydrated amorphous $LiBO_2$ to γ-$LiBO_2$ at different pressures. The DTA exothermic peaks also shifted toward lower temperature with increase in pressure, implying the phase transition temperature decreases with increase in applied pressure. The applied pressure can lower the crystallization condition. The DTA curves, however, are apparently different from that performed on α-$LiBO_2$ and become sharper with increase in pressure, suggesting shorter time for the completion of the phase evolution in amorphous $LiBO_2$ hydrate at higher pressure. In our experiments, we also notice that the latent heat of the amorphous→γ transition is much larger than that of α→γ transition. Generally, the disorder–order process is

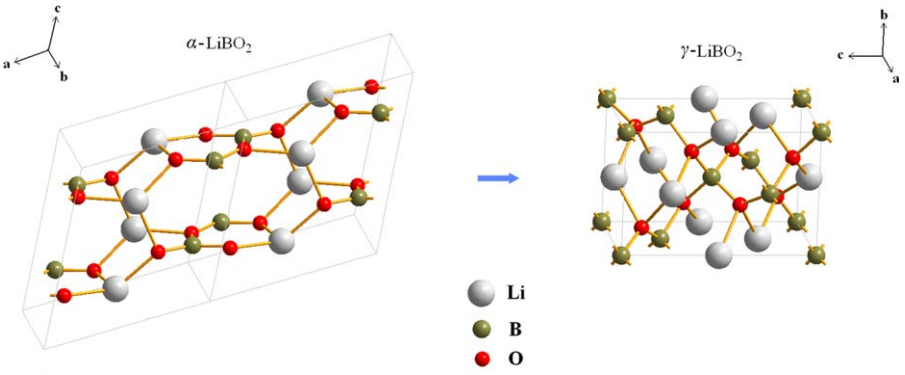

Fig. 5. A schematic diagram for the pressure-induced structural changes from triangle α-$LiBO_2$ to tetragonal γ-$LiBO_2$.

associated with bond breaking and formation, which manifested as the latent heat release (or absorption) in such first-order phase transition. In the case of amorphous→crystalline $LiBO_2$ transformation, crystallization process of amorphous $LiBO_2$ is profound and may involve much more bond formations than crystalline–crystalline phase evolution in α-$LiBO_2$.

In the present study, the melting curve of $LiBO_2$ has also been determined to 4.4 GPa. Fig. 6c presents the temperature signals of $LiBO_2$ samples at different pressures. An abrupt drop in each signal curve is clearly observed, implying the melting of $LiBO_2$ at that point. We find that these melting endothermic peaks shift towards higher temperature with increase in pressure, suggesting

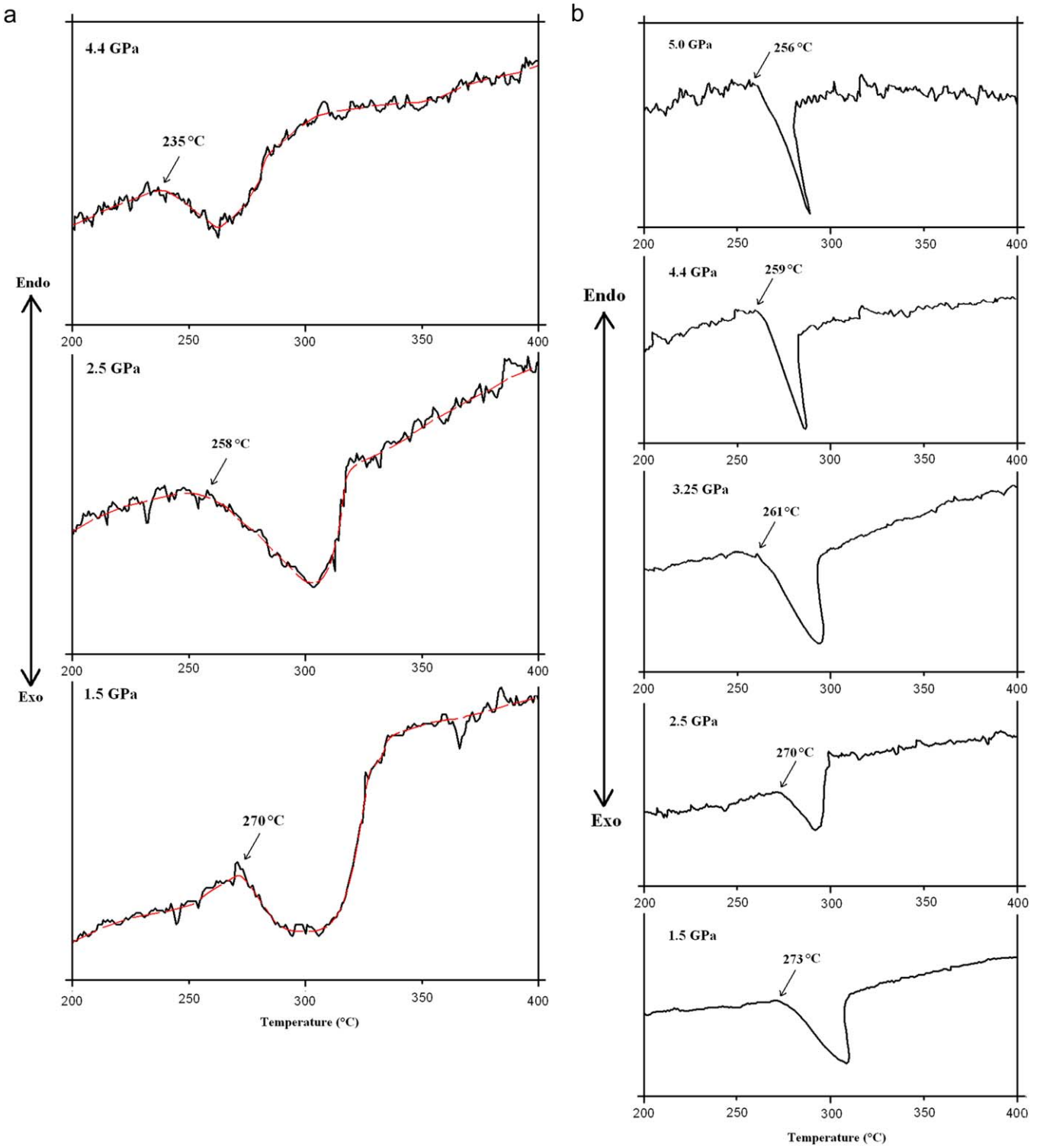

Fig. 6. (a) HP-DTA curves in the vicinity of structural transition from α- to γ-$LiBO_2$ at different pressures. The red dash lines are the fit for the curves. (b) HP-DTA curves in the vicinity of structural transition from dehydrated amorphous $LiBO_2$ to γ-$LiBO_2$ at different pressures. (c) Heating time dependence of temperature signals of $LiBO_2$ samples at different pressures. (d) HP-DTA curves in the vicinity of freezing point of $LiBO_2$ under different pressures. (For interpretation of the references to color in this figure legend, the reader is referred to the web version of this article.)

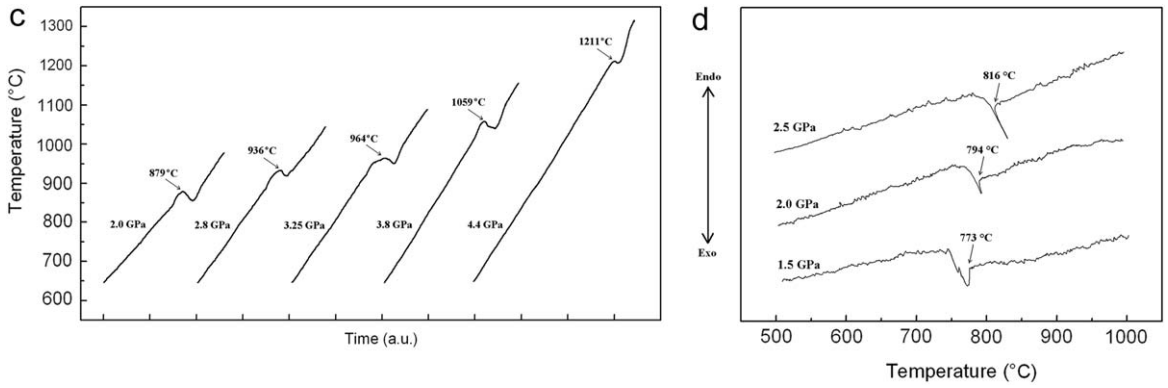

Fig. 6. (*Continued*)

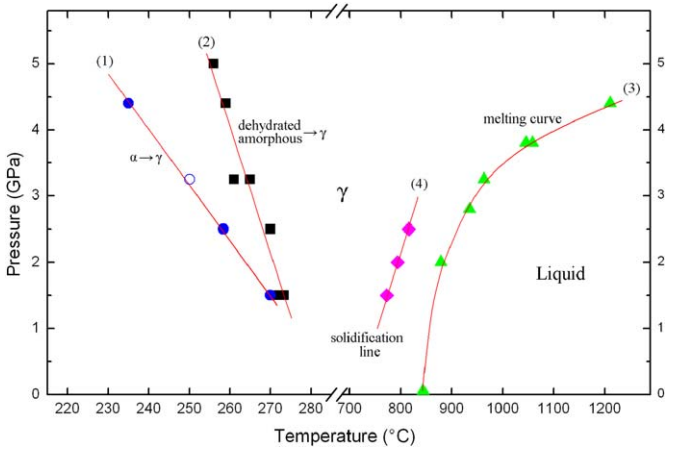

Fig. 7. Pressure–temperature phase transition diagram for $LiBO_2$ determined by *in-situ* HP-DTA and XRD. The symbols indicate the conditions for the following key observations: circles for the conditions of phase transition from α-$LiAlO_2$ to γ-$LiAlO_2$, among which open circle is the *ex-situ* XRD result shown in Fig. 1; squares for the onset temperature of the phase transition from dehydrated amorphous $LiBO_2$ to γ-phase; and triangles for the melting points of $LiBO_2$. Line 1 is the phase boundary line between α- and γ-phase, line 2 indicates the phase boundary line between dehydrated amorphous $LiBO_2$ and γ-$LiBO_2$, lines 3 and 4 are the melting curve and solidification line of $LiBO_2$, respectively.

the melting point of $LiBO_2$ increased with pressure. Moreover, the solidification line of $LiBO_2$ has also been determined in this work. Fig. 6d presents the HP-DTA curves in the vicinity of freezing point of $LiBO_2$ under different pressures. These solidification exothermic peaks become sharper and shift towards higher temperature with increase in pressure, suggesting the freezing point of $LiBO_2$ increased with pressure and shorter time for the completion of the solidification in $LiBO_2$ at higher pressure.

Based on the experimental observations discussed in the preceding paragraphs, the phase boundaries of $LiBO_2$ in the P–T space are plotted in Fig. 7. Line 1, which has a smaller negative P–T slope (dP/dT), is the phase transition boundary line between α- and γ-$LiBO_2$; and line 2, which has a larger negative P–T slope, is the phase transition boundary line between dehydrated amorphous $LiBO_2$ and γ-$LiBO_2$. Experimentally, the pressure dependence of the α→γ and amorphous→γ transition temperatures (dT/dP) are estimated to be −12.07 and −4.86 K/GPa, respectively. Since the volume change ($\Delta V_{\alpha\to\gamma} = -5.56\times10^{-6}\,m^3/mol$) for α→γ transformation at ambient condition is known, if we neglect the compressibility for the both phases under high pressure, the entropy change ($\Delta S_{\alpha\to\gamma}$) can be calculated to be 460.65 J/(mol K) using the Clausius–Clapeyron equation ($dP/dT = \Delta S/\Delta V$). Line 3, which has larger positive slope in the lower-pressure region and smaller positive slope in the higher-pressure region, is the melting curve of $LiBO_2$. As can be seen from Fig. 7, the melting point of $LiBO_2$ increases with pressure, the increasing tendency being more pronounced at higher pressure ranges. The well-known Simon functional form $a\,(1+bP)^c$ is now fit to the experimental melting points with the final result as follows [30]:

$$T_m(P) = 1118(1-0.22P)^{-0.084} \quad (1)$$

where T_m is the melting temperature in K and P is the pressure in GPa. Coincidently, the melting curve obtained in this work is in approximate agreement with the one deduced from our early experiments [31]. Line 4, which has a positive slope ($dT/dP = 43$ K/GPa), is the solidification line of $LiBO_2$. At the heating/cooling rate of 100 °C/min, the experimental undercooling of $LiBO_2$ is calculated to be around 85 °C at high pressures [32].

From Fig. 7, we note that the conditions for transformation from α- to γ-$LiBO_2$ are lower than that necessary to transform amorphous $LiBO_2$ hydrate to γ-$LiBO_2$. One of the possible reasons for the difference of the two densification processes is that, owing to the particular structure of α-$LiBO_2$, the BO_3 chains show two-dimensional stacking, the BO_4 units are easily formed at the expense of BO_3 units of the mutual parallel chains at high pressure, the content of BO_4 units increases with increase in pressure, and the α→γ transition temperature evidently decreases with increase in pressure. Another possible reason is that, considerable H_2O content and existence of $^{[3]}$B–O–$^{[3]}$B rings in the amorphous $LiBO_2$ hydrate may have significant effect on the amorphous→γ densification process. Previous first-principles molecular dynamics simulations study on boroxol rings in liquid and vitreous B_2O_3 reveals that the role played by $^{[3]}$B–O–$^{[3]}$B rings is to allow the B–O network to maintain a low-energy structure while keeping a relatively low density [33]. The amorphous→γ densification process with respect to B–O rings apparently involves two significant stages: rupture of B–O rings and conversion from $^{[3]}$B to $^{[4]}$B. the possible schemes is as follows:

$$\text{Ring}(^{[3]}\text{B}) \to \text{Nonring}(^{[3]}\text{B}) \to {}^{[4]}\text{B} \quad (2)$$

It has been reported that the standard enthalpy for the $^{[3]}$B to $^{[4]}$B conversion was estimated to be in the range 13–37 kJ/mol, whereas a similar value was estimated to be 27 kJ/mol for the enthalpy of rupture of $^{[3]}$B–O–$^{[3]}$B rings [34]. It can be deduced that the required transition activation energy for amorphous $LiBO_2$ is larger than that of α-$LiBO_2$. Therefore, the existence of $^{[3]}$B–O–$^{[3]}$B rings in the framework of amorphous solid may also increase the energy barrier for densification process of dehydrated amorphous $LiBO_2$.

Conventionally, alkali borate glasses are synthesized by melting the alkali borate powder at a temperature above the

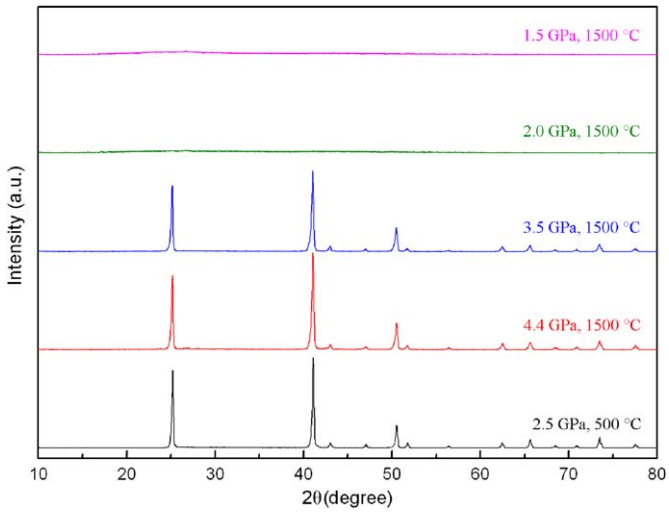

Fig. 8. XRD patterns for $LiBO_2$ samples quenched from melts at different pressures. For comparison, a γ-$LiBO_2$ sample quenched at 2.5 GPa and 500 °C is shown here.

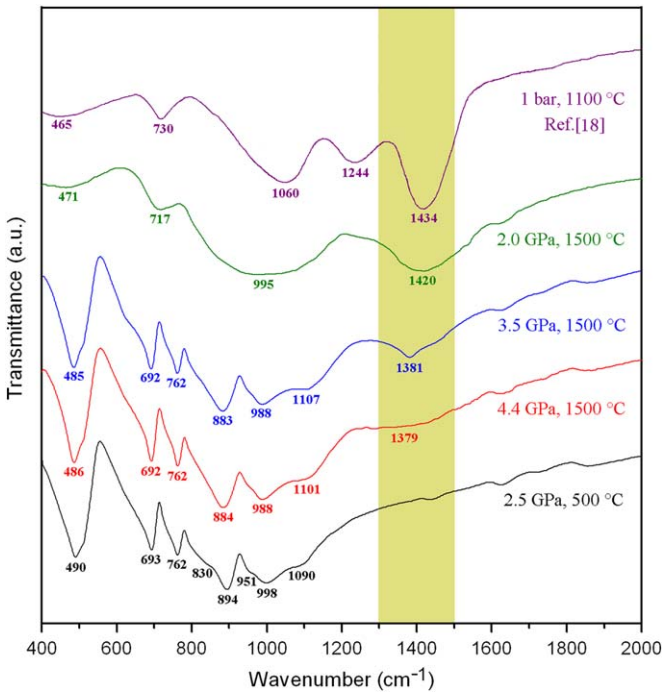

Fig. 9. IR absorption spectra for $LiBO_2$ samples quenched from melts at different pressures. For comparison, the γ-$LiBO_2$ is also shown here. (For interpretation of the references to colour in this figure legend, the reader is referred to the web version of this article.)

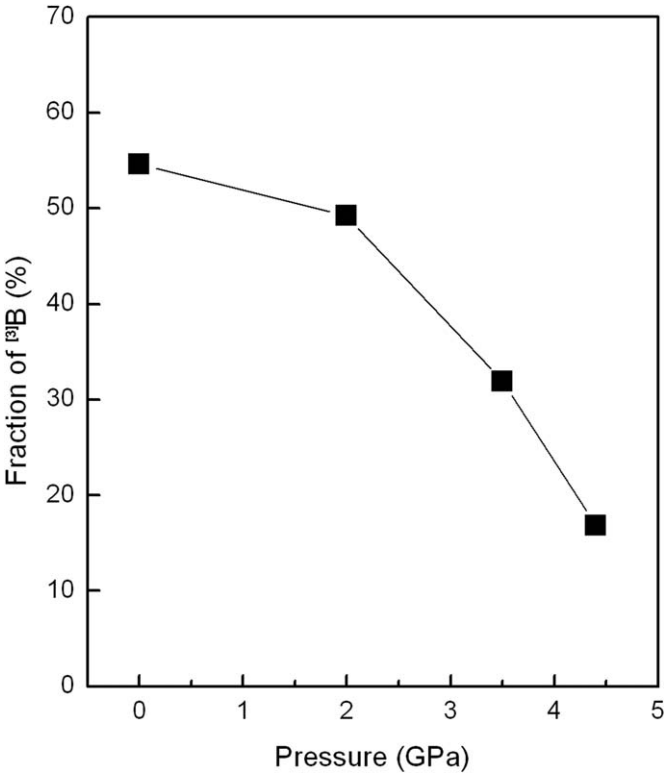

Fig. 10. Fraction of $^{[3]}B$ for quenched $LiBO_2$ with increasing pressure.

melting point and quenching at ambient pressure. In this present work, $LiBO_2$ was heated to the temperature of 1500 °C, where $LiBO_2$ was melt, and then quenched with a nearly same cooling rate about 50–60 °C/s. The XRD patterns of $LiBO_2$ samples quenched from melt at varying pressures up to 4.4 GPa are shown in Fig. 8; the XRD pattern for pure γ-$LiBO_2$ quenched at 2.5 GPa and 500 °C is shown here for comparison. In Fig. 8, the samples quenched from melts at higher pressures crystallize with a tetrahedral structure, while those quenched at lower pressures appear to be disordered by XRD. For further insight, Fig. 9 presents the IR absorption spectra for the corresponding samples in Fig. 8. For comparison, the IR spectra for γ-$LiBO_2$ quenched at 2.5 GPa and 500 °C as well as glassy $LiBO_2$ quenched at ambient pressure are also shown here [18]. Although XRD suggested that the samples quenched from melt at 3.5 and 4.4 GPa are just the pure phase of γ-$LiBO_2$, BO_3 units still is found in the quenched samples, evidenced by the observation of the absorption bands in the region 1300–1450 cm^{-1} (highlight in yellow), which is attributed to B–O band stretching of BO_3 units. It seems that some kind of amorphous $LiBO_2$ phase (with both BO_3 and BO_4 units) might coexist with crystalline γ-$LiBO_2$ (with only BO_4 units) in the sample solidified from melt. As shown in Fig. 9, the intensity of absorption peaks for BO_3 units decreases with increase in pressure, implying the fraction of $^{[3]}B$ decreases with increase in pressure while the fraction of $^{[4]}B$ increases with increase in pressure. The ~1000 and ~1400 cm^{-1} IR absorption peaks are characteristic of BO_4 and BO_3 groups, respectively, and it also can be used to examine the variation of their relative intensities in the IR spectra by considering their intensities as simply proportional to the amplitudes. It has been shown that the variation of boron species calculated by this method is very consistent with the one obtained from NMR experimental data [35]. Therefore, the fraction of $^{[3]}B$ in total coordinated B atoms ($^{[3]}B$+$^{[4]}B$) can be obtained by calculating the ratio $A_{\sim 1400 cm^{-1}}/(A_{\sim 1400 cm^{-1}} + A_{\sim 1000 cm^{-1}})$, where A refers to the amplitude of the IR peak. Fig. 10 presents the fraction of $^{[3]}B$ with pressure obtained from the IR absorption spectra as shown in Fig. 9. The $^{[3]}B$ fraction decreases with increase in pressure, whereas the decrease is not linear. At quenching pressure above 2 GPa, it dramatically decreases with pressure. The samples quenched from the melt at higher pressure have a greatly increased fraction of $^{[4]}B$. The cooling rate may affect the species and quantities of B–O units in the quenched sample. At a constant cooling rate of about 50–60 °C/s, $LiBO_2$ samples quenched from melts may undergo a glass transition at high pressure, representing the supercooled liquid frozen below the glass-transition temperature at high pressure. It was considered that the processes of quenching from melts under high pressure are very complex and depend on solidification history, as well as the chemical transformations between the

metaborate polymorphs that occur upon quenching. In our experiments, upon quenching from higher pressure, the formation of crystalline tetragonal γ-$LiBO_2$ is kinetically preferred. It can be assumed that the $LiBO_2$ melt at higher pressure may contain more $^{[4]}B$ fraction than the one at lower pressure.

As shown in Fig. 9, the IR absorption bands of the glass $LiBO_2$ quenched from melt at 2.0 GPa located in the regions 800–1100 and 1300–1450 cm^{-1}, suggesting this glass contains considerable both BO_3 and BO_4 units. Nevertheless, the IR spectra of this kind of $LiBO_2$ glass are different from that of the dehydrated amorphous $LiBO_2$ and the $LiBO_2$ glass prepared at ambient pressure [18]. Since no absorption band is observed at about 1250 cm^{-1}, the glassy $LiBO_2$ quenched from melt at high pressure may not contain $^{[3]}B$–O–$^{[3]}B$ rings, which is quite different from the $LiBO_2$ glass prepared at ambient pressure [18] and the glassy B_2O_3 quenched by melts at high pressures [20]. It is considered that high pressure may retard the formation of $^{[3]}B$–O–$^{[3]}B$ rings.

4. Conclusion

In conclusion, we report a direct experimental evidence for the pressure-induced coordination changes in the $LiBO_2$ system. The *in-situ* HP-DTA, XRD and IR spectra show a transformation from tri-coordinated to tetra-coordinated boron, forming dense tetrahedral $LiBO_2$. After decompression from high pressure, the tetra-coordinated bonding cannot revert back to the tri-coordinated state. However, the phase evolution conditions for crystalline α-$LiBO_2$ and amorphous $LiBO_2$ hydrate are different. In the particular structure of α-$LiBO_2$, considerable water content and the existence of $^{[3]}B$–O–$^{[3]}B$ rings in the amorphous $LiBO_2$ hydrate may contribute to the difference. A densification mechanism is proposed to elucidate the phase evolution in amorphous $LiBO_2$ hydrate. Our experiments also suggest that the $LiBO_2$ melts at lower pressure may contain more $^{[3]}B$ fraction than the one at higher pressure, but no evidence of the existence of $^{[3]}B$–O–$^{[3]}B$ rings. Upon quenching from higher pressure, the formation of crystalline tetragonal γ-$LiBO_2$ is kinetically preferred.

The results presented here provide insight into the nature of the coordination changes in $LiBO_2$ system and can help elucidate their densification mechanism. The method given here can easily be extended to other alkali borate systems and can provide possibilities for extensions to network oxides systems in general.

Acknowledgments

This project is supported by National Doctorial Research Foundation of China (Grant no. 20070610110) and National Natural Science Foundation of China (Grant no. 10772126).

References

[1] C.O. Ingamells, Anal. Chim. Acta 52 (1970) 323–334.
[2] P. Becker, Adv. Mater. 10 (1998) 979–992.
[3] C.D. Mcmillen, H.G. Giesber, J.W. Kolis, J. Crystal Growth 310 (2008) 299–305.
[4] S.K. Lee, P.J. Eng, H.K. Mao, Y. Meng, J. Shu, Phys. Rev. Lett. 98 (2007) 105502.
[5] B.T. Poe, P.F. McMillan, D.C. Rubie, S. Chakraborty, J. Yarger, J. Diefenbacher, Science 276 (1997) 1245–1248.
[6] J.L. Yarger, K.H. Smith, R.A. Nieman, J. Diefenbacher, G.H. Wolf, B.T. Poe, P.F. McMillan, Science 270 (1995) 1964–1967.
[7] J. Liang, X. Chen, J. Min, Z. Chai, S. Zhao, X. Cheng, Y. Zhang, G. Rao, Phys. Rev. B 51 (1995) 756–762.
[8] E. Bétourné, M. Touboul, Powder Diffr. 12 (1997) 155–159.
[9] N. Koga, T. Utsuoka, Thermochim. Acta 443 (2006) 197–205.
[10] M. Touboul, N. Penin, G. Nowogrocki, Solid State Sci. 5 (2003) 1327–1342.
[11] W.H. Zachariasen, Acta Crystallogr. 17 (1964) 749–751.
[12] A. Kirfel, G. Will, R.F. Stewart, Acta Crystallogr. B39 (1983) 175–185.
[13] M. Marezio, J.P. Remeika, J. Phys. Chem. Solids 26 (1965) 2083–2085.
[14] M. Marezio, J.P. Remeika, J. Chem. Phys. 44 (1966) 3348–3353.
[15] L. Lei, D. He, Y. Zou, W. Zhang, Z. Wang, M. Jiang, M. Du, J. Solid State Chem. 181 (2008) 1810–1815.
[16] J. Liang, Z. Chai, S. Zhao, Sci. Chin. 33A (1990) 105–112.
[17] X.M. Shi, Q. Wang, C.X. Li, X.J. Niu, F.P. Wang, K.Q. Lu, J. Crystal Growth 290 (2006) 637–641.
[18] G.D. Chryssikos, E.I. Kamitsos, A.P. Patsis, M.S. Bitsis, M.A. Karakassides, J. Non-Cryst. Solid 126 (1990) 42–51.
[19] C.P. Varsamis, A. Vegiri, E.I. Kamitsos, Phys. Rev. B 65 (2002) 104203.
[20] S.K. Lee, K. Mibe, Y. Fei, G.D. Cody, B.O. Mysen, Phys. Rev. Lett. 94 (2005) 165507.
[21] P.W. Mirwald, I.C. Getting, G.C. Kennedy, J. Geophys. Res. 80 (1975) 1519–1525.
[22] G.D. Chryssikos, M.S. Bitsis, J.A. Kapoutsis, E.I. Kamitsos, J. Non-Cryst. Solid 217 (1997) 278–290.
[23] C.H. Chang, J.L. Margrave, Mater. Res. Bull. 2 (1967) 929–933.
[24] E.I. Kamitsos, Phys. Chem. Glasses 44 (2003) 79–87.
[25] E.I. Kamitsos, M.A. Karakassides, G.D. Chryssikos, J. Phys. Chem. 90 (1986) 4528–4533.
[26] A.F.L. Almeida, I.F. Vasconcelos, M.A. Valente, A.S.B. Sombra, Physica B 322 (2002) 276–288.
[27] E.I. Kamitsos, M.A. Karakassides, G.D. Chryssikos, J. Phys. Chem. 91 (1987) 1073–1079.
[28] R.E. Youngman, J.W. Zwanziger, J. Am. Chem. Soc. 117 (1995) 1397–1402.
[29] H.P. Klug, L.E. Alexander, in: X-Ray Diffraction Procedures, Wiley, New York, 1974.
[30] F. Simon, G. Glatzel, Z. Anorg, Allgem. Chem. 178 (1929) 309.
[31] L. Lei, D. He, Cryst. Growth Des. 9 (2009) 1264–1266.
[32] B.A. Mueller, J.H. Perepezko, Metall. Mater. Trans. A 18 (1987) 1143–1150.
[33] G. Ferlat, T. Charpentier, A.P. Seitsonen, et al., Phys. Rev. Lett. 101 (2008) 065504.
[34] O. Majérus, L. Cormier, G. Calas, B. Beuneu, Phys. Rev. B 67 (2003) 024210.
[35] M. Ganguli, K.J. Rao, J. Phys. Chem. B 103 (1999) 920–930.